

A Raman-Structure Model for the Viscosity of SiO_2 - CaO - Al_2O_3 System



SHOKOUH HAGHDANI, MERETE TANGSTAD,
and KRISTIAN ETIENNE EINARSRUD

The relationship between structure and viscosity of molten slags is investigated using the Raman spectroscopy technique. To this end, a group of 20 synthetic slags in the SiO_2 - CaO - Al_2O_3 ternary system is considered. The slag compositions are close to industrial slags in silicon and ferrosilicon production, namely SiO_2 contents of 35 to 75 wt pct, CaO contents of 10 to 40 wt pct, and Al_2O_3 contents of 5 to 40 wt pct. Using a green source laser with 532 nm wavelength, the Raman spectra are measured within the wavenumbers on the order of 200 to 1300 cm^{-1} . To model viscosity using the Raman spectroscopy data, the ratio of low and high wavenumber vibrational bands is introduced as a structure-related Raman parameter (R). The Arrhenius equation is employed for the temperature dependency of the slag viscosity, where its parameters are linked to the R parameter through curve fitting. To model the relationship between structure and viscosity, experimental viscosity data are adopted from the literature. Comparing the model predictions and experiments, a good agreement is found between the model and measured values of viscosity.

<https://doi.org/10.1007/s11663-022-02483-9>
© The Author(s) 2022

I. INTRODUCTION

SILICATE melts are of great importance to Earth and material sciences, as well as metallurgical, cement, and glass industries dealing with materials that contain SiO_2 . For instance, in Earth science, magmas are admixtures of molten silicates, crystals, and gases. This silicate melt is responsible for both mass and heat transfer within the Earth and other terrestrial planets. In various high-temperature metallurgical processes, silicate slags as a combination of multiple oxides are formed during the operations, for instance, during the reduction of metal oxides in blast and electrical furnaces.^[1] Understanding and controlling the physical properties of silicate slags are necessary for improving the removal of molten slags and, thereby, the productivity of industrial operations.^[2,3] Among a wide variety of slag compositions, the SiO_2 - CaO - Al_2O_3 ternary system is of particular importance in the field of

metallurgy. This slag system is found in several metallurgical processes such as production of silicon and ferrosilicon,^[4-6] as well as the Al- and Ca-refining processes. The slag system is also of great importance for the iron and steel-making processes^[7-11] indicates its technological importance.

Physical properties of silicate melts such as thermal or electrical conductivity, density, and viscosity are directly linked to the atomic structure of the melt,^[12-15] and as such knowledge of the structure of silicate melts allows for further insights into the macroscopic properties of melt systems.^[16-25] In metal production processes, viscosity is an important property which influences for instance the metal-slag separation efficiency directly, and also heat and mass transfer within the furnace and processing operations.

Silicate glasses are widely employed as structural models for their molten counterparts because of the difficulty of studying the structural properties of melts. When a molten slag is quenched at a high cooling rate, the produced glass shows similar structural properties to that of the molten phase.^[12,26] On the other hand, there are various spectroscopic techniques to extract structural information of amorphous silicate glasses. For example, Raman spectroscopy is a powerful method, which has been popularly employed to provide valuable knowledge on the structural properties of melts and glasses.^[27-31] Therefore, the Raman spectroscopy measurements of silicate glasses can reveal the vibration units of molten slags and determine the structural

SHOKOUH HAGHDANI, MERETE TANGSTAD, and KRISTIAN ETIENNE EINARSRUD are with the Department of Materials Science and Engineering, Norwegian University of Science and Technology (NTNU), 7491, Trondheim, Norway. Contact e-mail: shokouh.haghdani@ntnu.no

Manuscript submitted September 26, 2021; accepted February 24, 2022.

Article published online March 28, 2022.

combinations of silicate melts. The Raman spectroscopy discloses existing vibrational modes and their relative distribution in glass through peak shift and intensity of the Raman spectrum. Thus, this technique can provide valuable understandings of the possible structural modifications and reliable predictions for macroscopic properties of glasses. In the last forty years, there have been extensive Raman spectroscopic investigations on the effect of basic and amphoteric oxides on the structure of silicate glasses containing alkali and alkali-earth elements.

Despite extensive efforts, generalizable prediction models for multicomponent melts properties as functions of temperature and composition remain a complicated task. There are numerous models in the literature trying to predict temperature and composition (structure) dependency for the viscosity of silicate melts. The temperature dependency of viscosity is usually given by the Arrhenius relationship, Weymann–Frenkel (WF) equation,^[32] or Vogel–Fulcher–Tammann (VFT) function.^[33–35] Fully empirical models have been suggested based on the mathematical description of selected experimental data.^[36,37] For the description of composition dependency of viscosity, two categories of methods have been developed, namely models based on bulk chemical composition^[38–42] and melt’s internal structure^[43–46] (non-structure- and structure-based models). Recently, Giordano and Russell,^[47] following Mercier et al.,^[48,49] presented a model for predicting melt viscosity using a single parameter taken from Raman spectroscopic measurements on glasses corresponding to multicomponent silicate melts preserved on Earth and other planets. The Raman parameter is calculated as the ratio of low and high wavenumber vibrational bands of the silicate glasses using a green source laser with 514.5 nm wavelength ($R_{514.5}$). The intensity of different Raman bands is related to the identity and abundance of structural species in the glasses. Thus, this model correlates the structural properties of the multicomponent glasses to the viscosity of their corresponding melts. The VFT function was employed for temperature dependency of viscosity where its coefficients were correlated to the $R_{514.5}$ parameter. The calibration dataset for this empirical model included 413 high-temperature viscosity measurements on 23 melt compositions (including sub-alkaline, calc-alkaline, alkaline, and peralkaline melts) for which Raman spectra were already published.^[48,49] The measured viscosities vary from $\sim 10^{-0.2}$ to 10^{12} Pa s over a temperature range of ~ 600 to 1650 °C. Following this work, a generalized model was proposed for the removal of Raman spectral dependency upon instrument type and setup for a calibration dataset of 30 multicomponent anhydrous silicate glasses.^[50] To this end, Raman ratios obtained in four different laboratories were normalized to a single standard parameter (R_n) through dividing to the highest Raman ratio value. The obtained results show a promising model to predict the melt viscosity solely using Raman measurements for multicomponent silicate glasses.

In this paper, we employ the Raman spectroscopy method to study slag structure information for a set of 20 synthetic slags in the $\text{SiO}_2\text{-CaO-Al}_2\text{O}_3$ system, thereby extending the silicate glasses considered by^[47,50] to compositions relevant to metallurgy. Following previous works,^[47,50] the Raman parameter (R) is obtained as the ratio of low and high wavenumber vibrational bands in the range of 200 to 1300 cm^{-1} for each slag composition. Another parameter taken from Raman spectra is the center of the Raman peaks in high wavenumber range (C_{HW}) cm^{-1} . The variations of structural parameters, namely R and C_{HW} , and slag viscosity are plotted against SiO_2 wt pct, CaO wt pct, and Al_2O_3 wt pct. The influence of SiO_2 , CaO , and Al_2O_3 oxides on both Raman parameters and viscosity values are discussed in detail. For this group of slags, we investigate the correlation between the R parameter and parameters calculated from slag chemical compositions such as basicity ($\text{CaO}/(\text{SiO}_2 + \text{Al}_2\text{O}_3)$), optical basicity,^[17] and non-bridging oxygen per tetrahedral cations (NBO/T).^[17] It is found that R is strongly correlated to the chemical parameters where the R values are reduced by increasing basicity, optical basicity, and NBO/T. In addition, these compositional parameters have been illustrated to be correlated to physical properties such as viscosity.^[17,51,52] To model slag viscosity and accounting for these correlations, the R parameter is linked to the measured viscosity values taken from the literature.^[53] We use the Arrhenius equation to present the temperature dependency of the viscosity where its parameters are correlated to the R values through curve fitting. Our findings show that the predictions of the constructed model are in a good agreement with the measured viscosity values.

The paper is organized as follows. In Section II, the sample preparation, characterization techniques, and Raman spectra analysis are presented. In Section III, the obtained results for the $\text{SiO}_2\text{-CaO-Al}_2\text{O}_3$ ternary system are discussed, and the relationship between slag structure and viscosity is formulated through a Raman-structure model for the viscosity. Finally, we summarize our findings and give concluding remarks in Section IV.

II. EXPERIMENTAL PROCEDURE

A. Sample Preparation

In the $\text{SiO}_2\text{-CaO-Al}_2\text{O}_3$ ternary system, 20 slag compositions were selected based on the slags produced in a silicon submerged arc furnace. The SiO_2 and CaO oxides are network-former and network-breaker oxides support polymerization and depolymerization of the silicate network, respectively. The role of Al_2O_3 is more complicated because Al_2O_3 can behave acidic or basic, depending on the amount of the two other oxides. For acidic slags, with a low CaO content, Al_2O_3 behaves as a basic oxide, while for basic slags, Al_2O_3 behaves like an acidic oxide. When sufficient CaO is available, the excess of cation Ca^{2+} balances the $(\text{AlO}_4)^{5-}$ charges. Hence,

Al₂O₃ operates as an acidic oxide and moves into the silicate network. Note that the cation units, used for charge balancing, cannot act as network-breakers.^[19]

Table I displays the designed compositions to investigate through the Raman spectrometer, with SiO₂ contents of 35 to 75 wt pct, CaO contents of 10 to 40 wt pct, and Al₂O₃ contents of 5 to 40 wt pct. To demonstrate the role of the SiO₂, CaO, and Al₂O₃ oxides on slag structure, the slag compositions are divided into groups where the content of one of these oxides is fixed and the contents of the two other oxides are exchanged. For example, the slag samples are categorized into 7 different groups where the content of CaO is fixed while SiO₂ is substituted by Al₂O₃.

The slag samples were synthesized using the analytical reagent oxides of SiO₂ (99.50 pct purity), CaO (99.95 pct purity), and Al₂O₃ (99.00 pct purity). To improve the accuracy of experiments, the CaO reagent was calcined at 1273 K for 2 hours in a muffle furnace to decompose any hydroxides. Then the powders were precisely weighted according to the designed compositions shown in Table I and mixed to obtain homogeneous mixtures. 60 g of the mixed powders were melted in a platinum crucible at 1943 K for 2 hours in a muffle furnace to homogenize the slag melts. After 2 hours, the crucible was pulled out from the furnace, and the molten slags were quickly poured into water and quenched to a glassy state. The slag quenching procedure was done fast so that the temperature of molten slags was still well above their melting point to obtain a fully amorphous phase. The mass of quenched slags was around 15 to 45 g depending on slag compositions. Finally, around 10 g of the quenched slags were grinded to use by characterization techniques described in Section II-B.

B. Characterization Techniques

We employed X-ray fluorescence (XRF), X-ray diffraction (XRD), and Raman spectroscopy techniques to analyze the prepared samples. Table I presents both designed and XRF compositions in wt pct, where XRF data were normalized to 100 pct. The chemical compositions from both designed and XRF analysis are also illustrated on a ternary phase diagram in Figure 1. As seen, the deviations between these values are minor, namely ± 0.2 to 2.8 pct. Note that the compositions from XRF analysis are used in the following sections.

The XRD results for slags S1 to S10 with the CaO contents of 10 to 25 wt pct and slags S11 to S20 with the CaO contents of 30 to 40 wt pct are shown in Figures 2(a) and (b), respectively. Figure 2 confirms that the quenched samples are in the glassy phase because there are no crystalline peaks in the XRD patterns. The presence of crystalline phases can influence the Raman spectra and potentially alter the composition of the remaining glassy phase.

Raman spectra measurements were performed to investigate the relationship between the slag structure and viscosity. Raman spectra of the prepared samples were measured using a laser confocal Raman

Table I. Designed and Measured Chemical Compositions Weight Percent of the SiO₂-CaO-Al₂O₃ system

Slag	Designed			XRF		
	SiO ₂	CaO	Al ₂ O ₃	SiO ₂	CaO	Al ₂ O ₃
S1	75	10	15	73.7	10.2	16.1
S2	70	10	20	72.7	8.9	18.4
S3	60	15	25	59.1	15.1	25.8
S4	70	20	10	68.2	21.2	10.6
S5	65	20	15	63.1	21.1	15.8
S6	60	20	20	58.4	20.7	20.9
S7	55	20	25	53.4	20.5	26.1
S8	45	20	35	45.5	19.3	35.2
S9	60	25	15	59.4	24.6	16.0
S10	35	25	40	35.8	24.1	40.1
S11	65	30	5	64.7	29.6	5.7
S12	60	30	10	59.9	29.3	10.8
S13	55	30	15	54.8	28.9	16.3
S14	50	30	20	49.9	29.4	20.7
S15	45	30	25	45.2	29.2	25.6
S16	60	35	5	58.8	34.8	6.4
S17	55	40	5	53.4	41.4	5.2
S18	50	40	10	48.6	41.0	10.4
S19	45	40	15	43.7	40.7	15.6
S20	40	40	20	39.2	39.6	21.2

spectrometer (WITec Alpha 300R, Germany) with a wavelength of 532 nm. The Raman spectra were collected in the range of 200 to 1300 cm⁻¹ at room temperature.

1. Analysis of Raman Spectra

In Figures 3(a) and (b), raw Raman spectra are shown for slags S1 to S10 (with the CaO contents of 10, 15, 20, and 25 wt pct for slags S1 and S2, S3, S4 to S8, S9 and S10, respectively) and slags S11 to S20 (with the CaO contents of 30, 35, and 40 wt pct for slags S11 to S15, S16, and S17 to S20, respectively). Figures 3(c) and (d) present normalized Raman spectra after baseline subtraction through the cubic baseline *B* method^[48] for slags S1 to S10 and slags S11 to S20, respectively. In this baseline correction procedure, first, the baseline is drawn between the two boundaries of spectra (180 to 280 and 1230 to 1600 cm⁻¹ regions) where no signal is available. Also, the baseline crosses one or two invariant domains in the intermediate region (650 and 850 cm⁻¹) between these two boundaries.^[48] Then, the baseline (or background) is removed from raw Raman data. Note that different baseline methods can produce significant differences in the topology of the extracted spectra, especially on the form of the intermediate range for slags with high CaO content. The performance of the cubic baseline *B* procedure has been examined comparing to other baseline methods^[48,50] It has been found that this method provides the best baseline fit in according to the ability of Raman parameter correlation to structural parameters and viscosity as described in Section III. The baseline fitting

procedure was performed using Fityk software which is an open-source software for data analysis and nonlinear curve fitting.^[54]

In the frequency range between 200 to 1300 cm^{-1} , the Raman spectra in aluminosilicate glasses possess two main bands that are broad and asymmetric. The first band is mainly localized between 200 and 700 cm^{-1} , centered at about 490 cm^{-1} , and sometimes a shoulder at 600 cm^{-1} (is so-called as low wavenumber (LW)). The second band concentrates between 800 and 1300 cm^{-1} with its peak located at about 960 cm^{-1} (is so-called high wavenumber (HW)). Also, at intermediate wavenumbers, a lower weight band can be detected between 650 and 850 cm^{-1} with a center about 800 cm^{-1} (is so-called as medium wavenumber (MW)). The LW band is mainly made by the Si-O-Si and Si-O⁻-Al bending vibrations, where O⁻ denotes bridging oxygen which is only connected to Si or Al cations (network-forming cations). In this region, a strong band

near 500 cm^{-1} (D1) and sometimes a shoulder near 600 cm^{-1} (D2) are assigned to breathing vibrations of 4- and 3-membered rings of the tetrahedral in the aluminosilicate network, respectively.^[55] The MW band is produced *via* the Si-O⁰ stretching mode, where its intensity corresponds to SiO₂ content. The HW band is generated by stretching vibrations Si-O⁻ bonds, where O⁻ denotes non-bridging oxygen and is bound to only one network-former cation (Ca-O⁻-Si). The observed feature of the HW region arises from the combined contributions of Qⁿ units where Q represents a SiO₄ tetrahedron and n is the number of O⁰ per tetrahedron, which can be between 0 to 4.^[56] These units are assigned to monomer structure (Q⁰), dimer structure (Q¹), chain structure (Q²), sheet structure (Q³), and a three-dimensional structure (Q⁴).^[57]

III. RESULTS AND DISCUSSION

A. Structure-Related Raman Parameter

To use the Raman spectroscopy data for demonstrating the relationship between slag structure and viscosity quantitatively, a Raman parameter, R , is introduced by the ratio of Raman intensity (I) of the two main bands of LW and HW as $R = I_{LW}/I_{HW}$.^[47,50] The center of the Raman peaks in HW range (C_{HW}) cm^{-1} is another parameter taken from Raman spectra to study the variation of slag structure by slag compositions. Shifting C_{HW} to the left-hand side, i.e., lower wavenumbers, indicates the depolymerization of the silicate network in slag structure while moving C_{HW} to the right-hand side, i.e., higher wavenumbers, displays the polymerization of the silicate network. The R values have been illustrated to be strongly correlated to the structural chemical parameters, e.g., basicity (B , $\text{CaO}/(\text{SiO}_2 + \text{Al}_2\text{O}_3)$), optical basicity (OB), and non-bridging oxygen per tetrahedral cations (NBO/T). NBO/T parameter is calculated

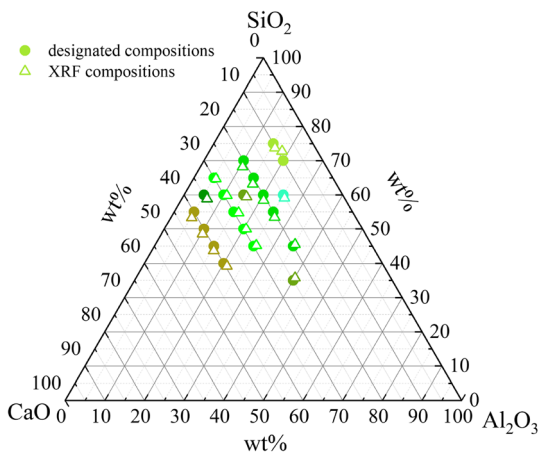


Fig. 1—Chemical compositions in ternary phase diagram of the SiO₂-CaO-Al₂O₃ system.

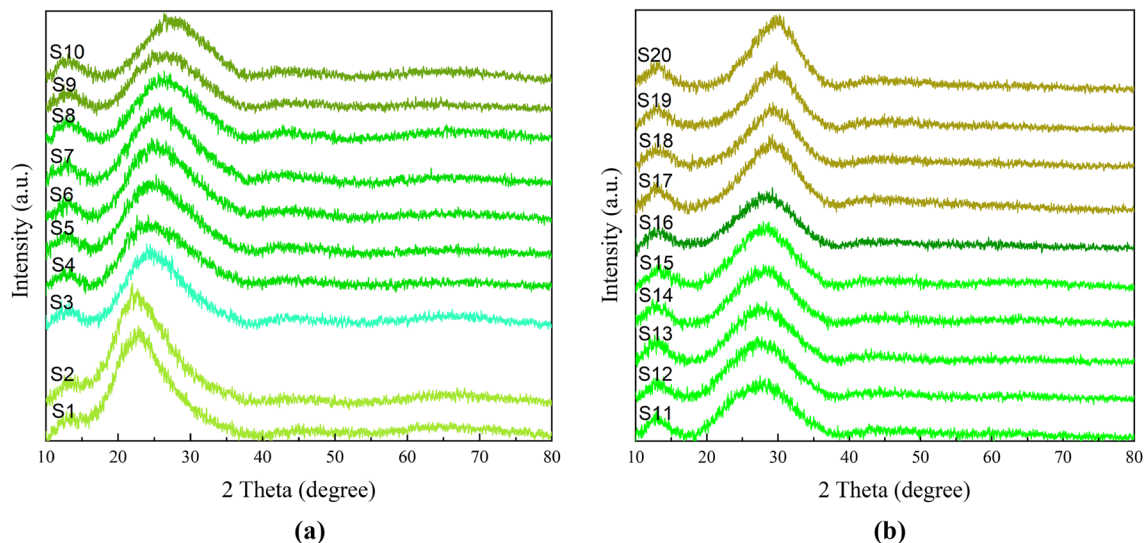


Fig. 2—XRD results for (a) slags S1 to S10 and (b) slags S11 to S20, respectively.

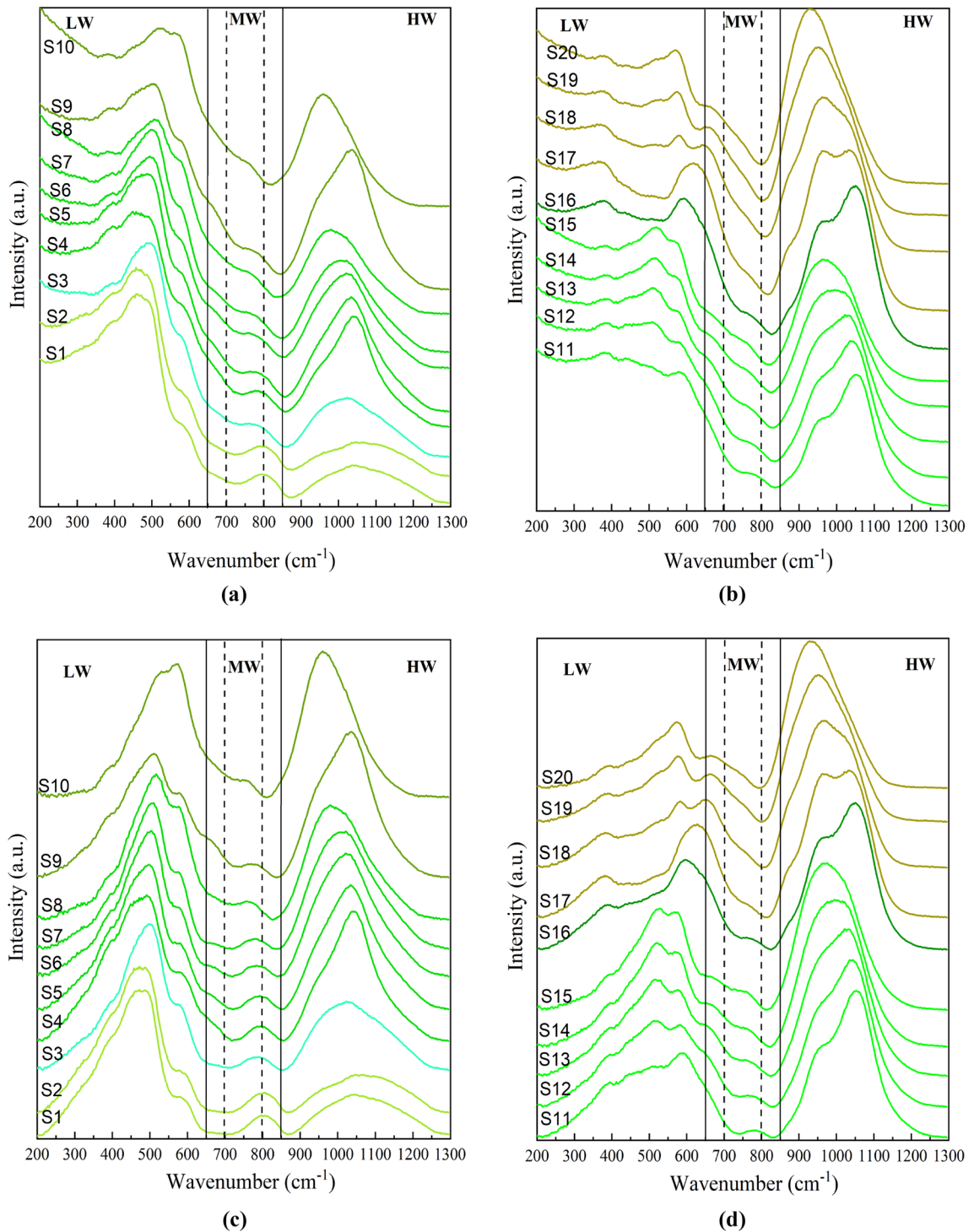


Fig. 3—(a) and (b) Raw Raman spectra for slags S1 to S10 and slags S11 to S20, respectively. (c) and (d) Normalized Raman spectra after baseline subtraction for slags S1 to S10 and slags S11 to S20, respectively.

from the chemical composition of silicate glasses and is known to be representative for the degree of polymerization of the silicate network. Table II presents chemical compositions from XRF analysis in mol pct, B, OB, NBO/T, R , and C_{HW} cm^{-1} values. Note that B, OB, and NBO/T parameters were calculated using XRF compositions in mol pct.

In Figures 4(a) through (c), R (I_{LW}/I_{HW}) values are plotted as a function of basicity, optical basicity, and NBO/T, respectively. While the R magnitudes vs NBO/T have been presented in previous works,^[47,50] here in this paper, we study the R parameter against basicity and optical basicity. As can be seen, the variations of R are relatively similar for both basicity and optical basicity.

Also, the R values are proportional with the composition-related parameters inversely and nonlinearly. Figure 4 shows that R reduces by increasing basicity, optical basicity, and NBO/T magnitudes, demonstrating that Raman R values correspond to the polymerization of the silicate network in melts and glasses.

The variations of R ($I_{\text{LW}}/I_{\text{HW}}$) and C_{HW} parameters against SiO_2 wt pct, CaO wt pct, and Al_2O_3 wt pct are presented in Figures 5 and 6, respectively. For the visualization purposes, the slags containing relatively similar contents of CaO wt pct (shown in Figures 5(a) and (e) as well as 6(a) and (e)), Al_2O_3 wt pct (shown in Figures 5(b) and (d) as well as 6(b) and (d)), and SiO_2 wt pct (shown in Figures 5(c) and (f) as well as 6(c) and (f)) are marked using same markers.

Figure 5(a) shows that the R values slightly change against increasing SiO_2 for the fixed content of CaO , which can point to the fact that the R parameter is strongly correlated to the CaO content. For slags containing approximately 20 wt pct CaO , i.e., slags S8 to S4, R only slightly reduces as 1.27, 1.25, 1.18, 1.17, and 1.13, respectively, by increasing SiO_2 from 45.5 to 68.2 wt pct. However, by increasing SiO_2 from 39.2 to 53.4 wt pct, R slightly grows for slags S20 to S17 containing approximately 40 wt pct CaO as 0.45, 0.45, 0.46, and 0.63, respectively. For slags S15 to S11 with approximately 30 wt pct CaO , R increases first and then reduces, namely 0.69, 0.70, 0.66, 0.59, and 0.58, respectively, by increasing SiO_2 from 45.2 to 64.7 wt pct. Figure 5(b) illustrates that the R values reduce slightly as 0.63, 0.61, and 0.58 for slags S17, S16, and S11, respectively, by increasing SiO_2 as 53.4, 58.8, and 64.7 wt pct, with the lowest amount of Al_2O_3 , approximately being 5 wt pct. In contrast, for slags containing a higher amount of Al_2O_3 , R increases by increasing SiO_2 . For example, the R values for slags S15, S7, and S3 with approximately 25 wt pct Al_2O_3 (25.6, 26.1, and 25.8 wt pct) increase to 0.69, 1.25, and 2.13 by increasing the SiO_2 as 45.2, 53.4, and 59.1 wt pct.

Figures 5(c) and (d) show that the increase of CaO from 10 to 30 wt pct sharply reduces R , whereas an increase in CaO from 30 to 40 wt pct changes this parameter slightly. As seen, in Figures 5(c) and (d), there are three clusters of slags with relatively close R values, which contain various contents of SiO_2 and Al_2O_3 , respectively. These clusters are made by slags S4 to S8, S11 to S15, and S17 to S20 that contain approximately 20, 30, and 40 CaO wt pct, respectively.

The variations of R against Al_2O_3 wt pct are illustrated in Figures 5(e) and (f) for different contents of CaO and SiO_2 , respectively. Figure 5(e) shows the same pattern as Figure 5(a) where the R values are slightly changed by increasing the Al_2O_3 content for those slags that host similar amount of CaO . However, the R values change inversely with respect to Al_2O_3 compared to its variations with increasing SiO_2 . For example, for those slags contain approximately 20 wt pct CaO (i.e., slags S4 to S8), R slightly increases as 1.13, 1.17, 1.18, 1.25, and 1.27, by increasing Al_2O_3 from 10.6 to 35.2 wt pct.

Also, Figure 5(f) exhibits a similar pattern as the one observed in Figure 5(b) where the R parameter increases against Al_2O_3 . Note that in Figure 5(f), the increase of the R parameter is more pronounced for slags containing higher amounts of SiO_2 .

Figure 6(a) displays that the C_{HW} values are increased by increasing SiO_2 for the fixed content of CaO . The increase of the C_{HW} parameter is more pronounced for slags S20 to S17 containing approximately 40 wt pct CaO as 928, 954, 968, and 1032 cm^{-1} , respectively. Figure 6(b) shows that the C_{HW} values increase first and then slightly are changed by increasing SiO_2 except for slags containing 20 wt pct Al_2O_3 , where C_{HW} is increased by increasing SiO_2 . For this group of slags, namely slags S20, S14, S6, and S2, C_{HW} increases as 928, 994, 1021, and 1069 cm^{-1} , respectively.

Figure 6(c) illustrates that the C_{HW} parameter behaves differently with increasing the CaO content for slags containing different content of SiO_2 . By increasing CaO , C_{HW} decreases for slags containing 45 and 50 wt pct SiO_2 while C_{HW} increases for slags containing 60 and 65 wt pct SiO_2 . For the fixed content of Al_2O_3 , Figure 6(d) indicates the C_{HW} parameter slightly changes first and then decreases by increasing the CaO content except for slags containing 20 wt pct Al_2O_3 .

The variations of C_{HW} with respect to Al_2O_3 wt pct are presented in Figures 6(e) and (f) for different contents of CaO and SiO_2 . In Figure 6(e), the C_{HW} values change inversely by increasing Al_2O_3 , compared to its variations with increasing SiO_2 presented in Figure 6(a). The decrease of the C_{HW} parameter is more pronounced for slags S17 to S20 containing approximately 40 wt pct CaO as 1032, 968, 954, and 928 cm^{-1} , respectively, by increasing Al_2O_3 from 5.2 to 21.2 wt pct. Figure 6(f) shows that the C_{HW} parameter acts differently by increasing the Al_2O_3 content for slags with different content of SiO_2 as seen in Figure 6(c). C_{HW} increases for slags containing 45 and 50 wt pct SiO_2 while C_{HW} reduces for slags containing 60 and 65 wt pct SiO_2 by increasing Al_2O_3 .

In general, we observe that the R and C_{HW} values are proportional to the SiO_2 content and inversely proportional to the CaO content. The influence of Al_2O_3 on the variations of R and C_{HW} parameters and thereby on the slag structure is more complicated. As seen in Figure 6(f), by increasing the Al_2O_3 content for slags with the fixed content of SiO_2 , the C_{HW} parameter increases for slags with low content of SiO_2 , while it decreases for high content of SiO_2 . These results demonstrate the amphoteric behavior of Al_2O_3 . For slags with low content of SiO_2 , Al_2O_3 acts as an acidic oxide since the C_{HW} parameter shifts to the higher wavenumbers. This means that the silicate network is polymerized by increasing Al_2O_3 . In contrast, Al_2O_3 acts as a basic oxide for slags with high content of SiO_2 , through shifting the C_{HW} parameter to lower wavenumbers which means depolymerization of the silicate network.

Table II. Chemical Composition mol Percent From XRF Analysis, B (Basicity), OB (Optical Basicity), NBO/T (Non-bridging Oxygen per Tetrahedral cations), R (Ratios of Intensity Heights (I) in LW and HW Regions, I_{LW}/I_{HW}), and C_{HW} cm^{-1} (Center of Raman Peaks in HW Range)

Slag	SiO ₂	CaO	Al ₂ O ₃	B	OB	NBO/T	R	C _{HW}
S1	78.31	11.64	10.04	0.13	0.50	0.03	3.64	1045
S2	78.14	10.24	11.62	0.11	0.49	− 0.03	3.86	1069
S3	65.28	17.93	16.78	0.22	0.51	0.02	2.13	1024
S4	70.21	23.34	6.45	0.30	0.54	0.40	1.13	1045
S5	66.46	23.77	9.77	0.31	0.54	0.32	1.17	1034
S6	62.86	23.92	13.22	0.31	0.54	0.24	1.18	1021
S7	58.88	24.16	16.95	0.32	0.53	0.15	1.25	1021
S8	52.39	23.74	23.87	0.31	0.53	0.00	1.27	981
S9	62.44	27.63	9.92	0.38	0.55	0.43	0.85	1037
S10	41.96	30.34	27.70	0.43	0.54	0.05	0.91	960
S11	64.83	31.81	3.35	0.47	0.57	0.79	0.58	1053
S12	61.29	32.17	6.54	0.47	0.57	0.69	0.59	1037
S13	57.44	32.46	10.10	0.48	0.57	0.57	0.66	1024
S14	53.36	33.63	13.00	0.51	0.57	0.52	0.70	994
S15	49.40	34.14	16.46	0.52	0.57	0.43	0.69	976
S16	58.88	37.35	3.76	0.59	0.59	1.01	0.61	1050
S17	52.93	44.00	3.06	0.78	0.62	1.38	0.63	1032
S18	49.26	44.55	6.18	0.80	0.62	1.24	0.46	968
S19	45.28	45.17	9.54	0.82	0.62	1.11	0.45	954
S20	41.65	45.08	13.27	0.82	0.62	0.93	0.45	928

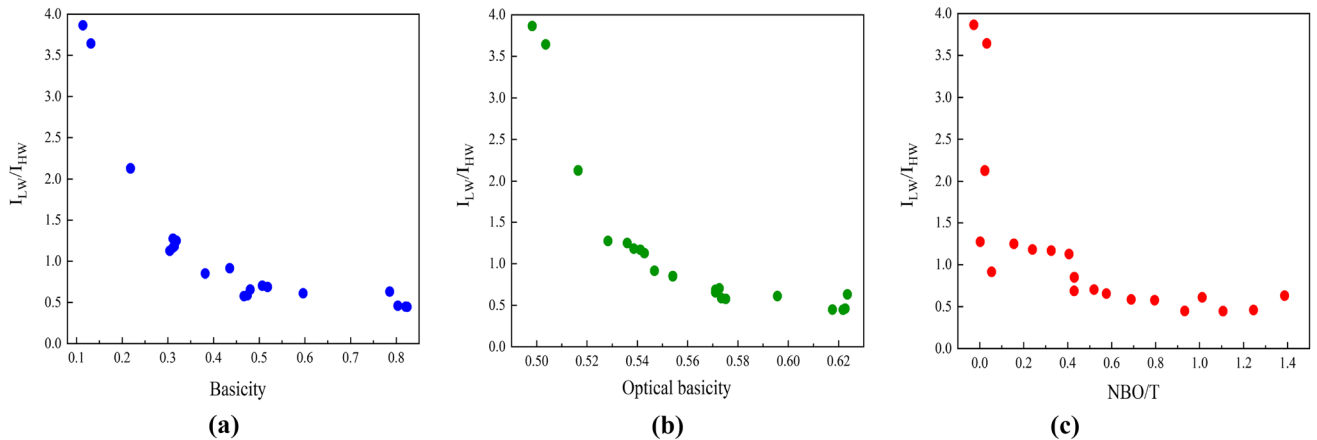


Fig. 4— R (I_{LW}/I_{HW}) vs (a) Basicity, (b) Optical basicity, and (c) NBO/T.

B. Raman-Structure Model: Relation Between Structure and Viscosity

In this section, the relationship between slag structure and viscosity is discussed using the R parameter (I_{LW}/I_{HW}). Table III presents the experimental viscosity values, η , for temperatures in the range of 1423 to 1773 K for all slags, which are adopted from the literature^[53] except for slags S1 and S8 that are unavailable.

Experimental viscosity data at 1773 K, $\log \eta$ Pa s are plotted as a function of SiO₂ wt pct, CaO wt pct, and Al₂O₃ wt pct in Figures 7(a) through (f). The presentation of the slags containing relatively similar contents of CaO wt pct, Al₂O₃ wt pct, and SiO₂ wt pct are the same as indicated in Figures 5 and 6. Figure 7(a) shows

that the $\log \eta$ values increase slightly by increasing the content of SiO₂ for the fixed content of CaO. Figure 7(b) shows the variations of $\log \eta$ against SiO₂ for slags with the fixed content of Al₂O₃. The $\log \eta$ values are increased by increasing SiO₂ for all groups of slags.

The variations of $\log \eta$ against CaO wt pct are shown in Figures 7(c) and (d) for slags with the fixed content of SiO₂ and Al₂O₃, respectively. Figures 7(c) and (d) illustrate that the increase of CaO from 10 to 30 wt pct sharply reduces the $\log \eta$ values while an increase in CaO from 30 to 40 wt pct reduces this parameter less. Figures 7(c) and (d) display that there are three clusters of slags with relatively close $\log \eta$ values. These clusters are made by slags S4 to S7, S11 to S15, and S17 to S20 that contain approximately 20, 30, and 40 CaO wt pct, respectively.

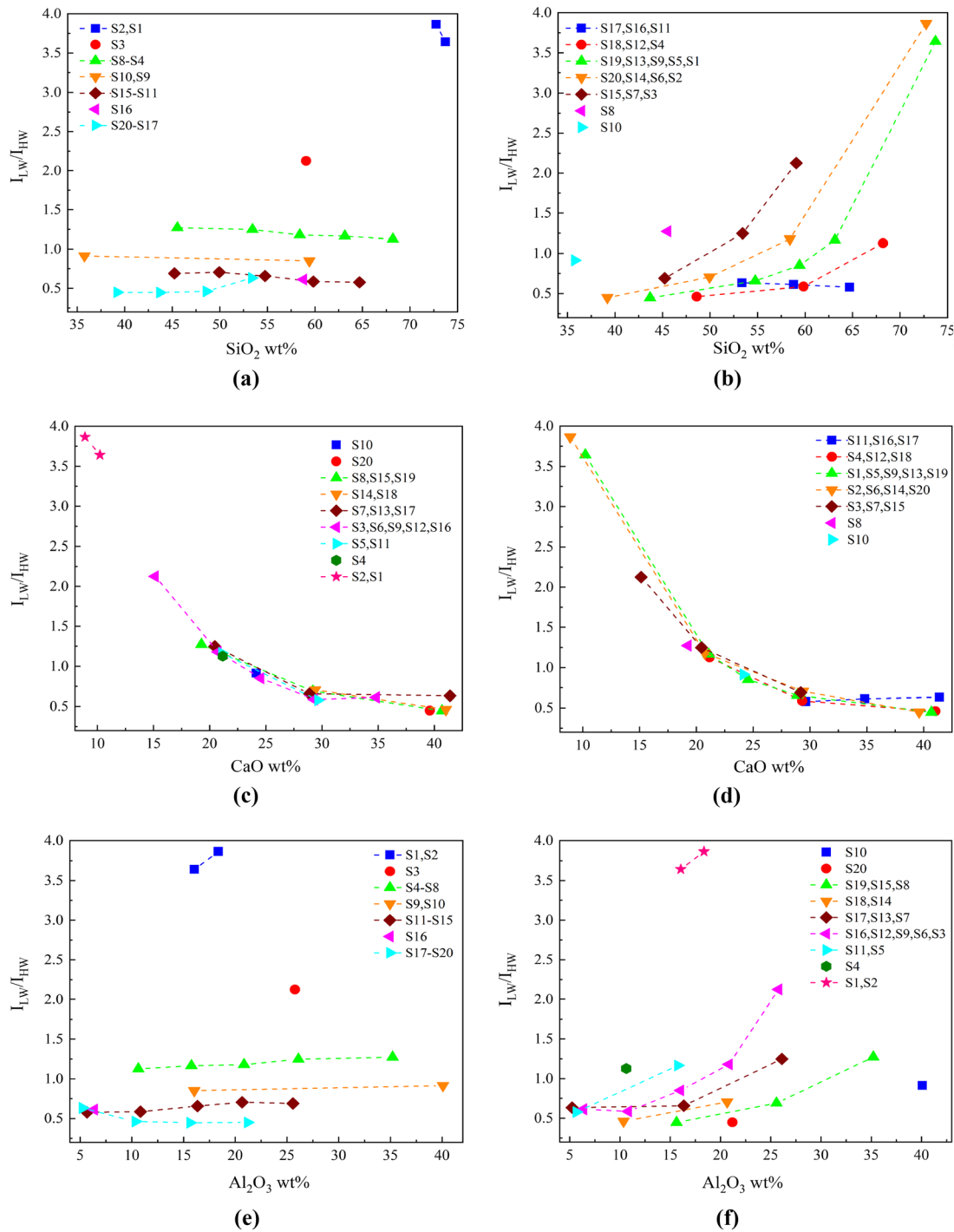


Fig. 5— R (I_{LW}/I_{HW}) vs SiO_2 wt pct (a) low to high contents of CaO wt pct and (b) low to high contents of Al_2O_3 wt pct. R (I_{LW}/I_{HW}) vs CaO wt pct (c) low to high (ls) of SiO_2 wt pct and (d) low to high contents of Al_2O_3 wt pct. R (I_{LW}/I_{HW}) vs Al_2O_3 wt pct for (e) low to high contents of CaO wt pct and (f) low to high contents of SiO_2 wt pct.

Figures 7(e) and (f) show the variations of $\log \eta$ against Al_2O_3 wt pct for various contents of CaO and SiO_2 , respectively. Figure 7(e) shows the same pattern as Figure 7(a) except that the $\log \eta$ values change inversely with respect to Al_2O_3 compared to its variations with increasing SiO_2 . Also, Figure 7(f) displays a similar pattern as the one observed in Figure 7(b) where the $\log \eta$ parameter increases against Al_2O_3 .

Figures 5 through 7 indicate that the pattern of the $\log \eta$ variations are similar to the variations of the R parameter against SiO_2 wt pct, CaO wt pct, and Al_2O_3 wt pct. For example, the $\log \eta$ and R values slightly change against increasing SiO_2 or Al_2O_3 for the fixed content of CaO. While, the $\log \eta$ and R values decrease with the increase of CaO for the fixed content of SiO_2 or Al_2O_3 . Similar to the R and C_{HW} parameters,

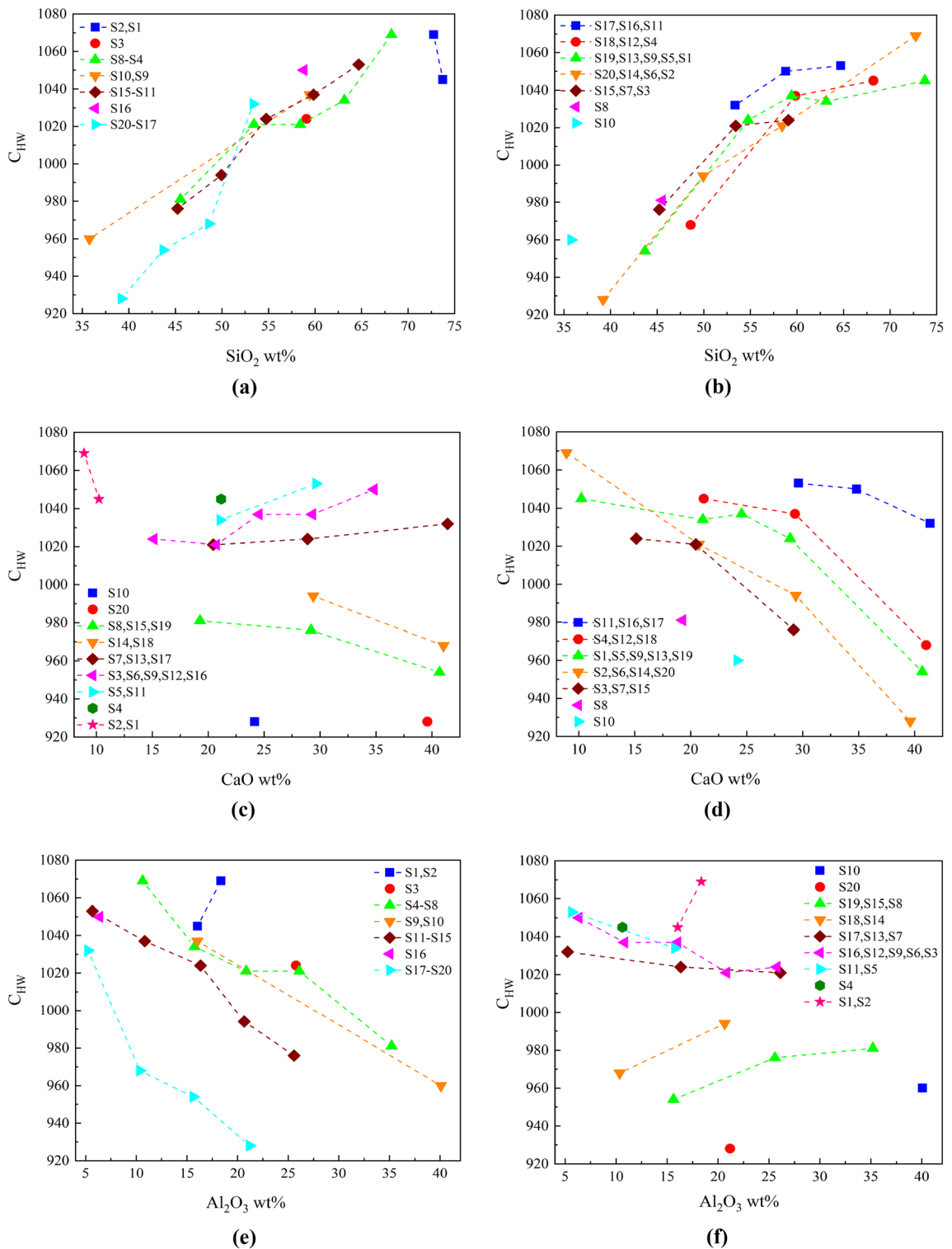


Fig. 6—Center of Raman peaks in HW range (C_{HW}) cm^{-1} vs SiO_2 wt pct (a) low to high contents of CaO wt pct and (b) low to high contents of Al_2O_3 wt pct. C_{HW} cm^{-1} vs CaO wt pct (c) low to high contents of SiO_2 wt pct and (d) low to high contents of Al_2O_3 wt pct. C_{HW} cm^{-1} vs Al_2O_3 wt pct for (e) low to high contents of CaO wt pct and (f) low to high contents of SiO_2 wt pct.

the $\log \eta$ values are proportional to the SiO_2 content and inversely proportional to the CaO content. While the amphoteric nature of Al_2O_3 can be seen from the

structural data, i.e., R and C_{HW} , the corresponding behavior cannot be found in the viscosity data presented here.

Table III. Viscosity Measurements (Pa s) From the Literature^[53] for Slags S1 to S20 (Expect for Slags S1 and S8)^[53]

Slag	Temperature K							
	1423	1473	1523	1573	1623	1673	1723	1773
S1								
S2				12800.00	4620.00	1820.00	827.00	395.00
S3						250.00	122.00	62.10
S4						107.00	60.00	36.10
S5				450.00	196.00	104.00	57.40	31.10
S6		1470.00	575.00	253.00	126.00	66.30	35.30	20.40
S7						66.00	31.70	17.30
S8								
S9	1060.00	373.00	156.00	73.00	39.10	21.40	12.80	7.77
S10							4.09	2.49
S11							6.99	4.22
S12	252.00	99.00	42.10	22.00	12.60	8.16	5.17	3.26
S13	278.00	108.00	45.60	22.50	12.10	7.32	4.48	2.86
S14			52.90	24.70	12.50	7.09	4.23	3.02
S15					13.20	7.01	4.10	2.63
S16						3.94	2.50	1.71
S17							1.28	0.84
S18						1.92	1.21	0.82
S19					3.31	1.94	1.25	0.85
S20			14.80	6.76	3.51	2.15	1.37	0.83

As was seen in Section III–A, the R parameter is strongly correlated to basicity, optical basicity, and NBO/T values. On the other hand, these composition-related parameters have been shown to be strongly correlated to physical properties such as viscosity^[7]. In Figures 8(a) through (c), $\log \eta$ is plotted against basicity, optical basicity, and NBO/T, respectively, for two temperatures of 1723 and 1773 K. Comparing Figures 4 and 8, one finds similar patterns for the variations of R (I_{LW}/I_{HW}) and $\log \eta$ against the mentioned parameters. Both R and $\log \eta$ values are reduced nonlinearly by increasing basicity, optical basicity, and NBO/T magnitudes. The demonstrated relationships among Raman R parameter, structural chemical parameters, and viscosity suggest that R values can be used to link and thereby predict the viscosity of silicate melts.

In this study, the Arrhenius equation is adopted for the temperature dependency of viscosity:

$$\log \eta = A + \frac{B}{T}, \quad [1]$$

in which A and B parameters are found through curve fitting. In Figure 9, model values of A and B , presented in Table IV, are plotted against the R values. The correlation between R and the A and B parameters shown in Figure 9 suggests the following expressions for the dependence of the A and B on R parameter:

$$A = a_1 + a_2 R, \quad [2]$$

and

$$B = b_1 R^{b_2}, \quad [3]$$

where a_1 , a_2 , b_1 , and b_2 , are adjustable parameters obtained through simultaneously fitting the model, namely Eqs. [1] through [3], to measured pairs of $\log \eta$ - T (K) given in Table III and R values shown in Table II for slags S1 to S20 (expect for slags S1 and S8). The magnitudes for a_1 , a_2 , b_1 , and b_2 parameters are obtained as -14.80 , -1.87 , 33943 , and 0.27 , respectively.

Finally to model the temperature dependency of silicate melt viscosity as a function of the Raman R parameter, the expressions of A and B are substituted in the Arrhenius equation, i.e., Eq. [1]

$$\log \eta = -14.80 - 1.87 R + \frac{33943 R^{0.27}}{T}. \quad [4]$$

The predicted viscosity values, obtained using Eq. [4], are plotted against the experimental viscosity data in Figure 10. Comparing the model predictions and experimental values, a good agreement is found between the modeled and measured viscosities for these slags. The Raman-structure model reproduces the measured viscosity within ± 0.5 log units for most of the slags. The largest deviations between the measured and predicted values are found for slags S10, S11, and S17. Note that for these slags, the viscosity values for only two temperatures 1723 and 1773 K were available in the literature, as presented in Table III, which causes this largest deviation. The inclusion of more viscosity data would improve the predictions by better adjusting the parameters of the model. In Figure 11, the predicted isothermal viscosity curves (1523 to 1773 K) as a function of R in the range of 0 to 4 are displayed using

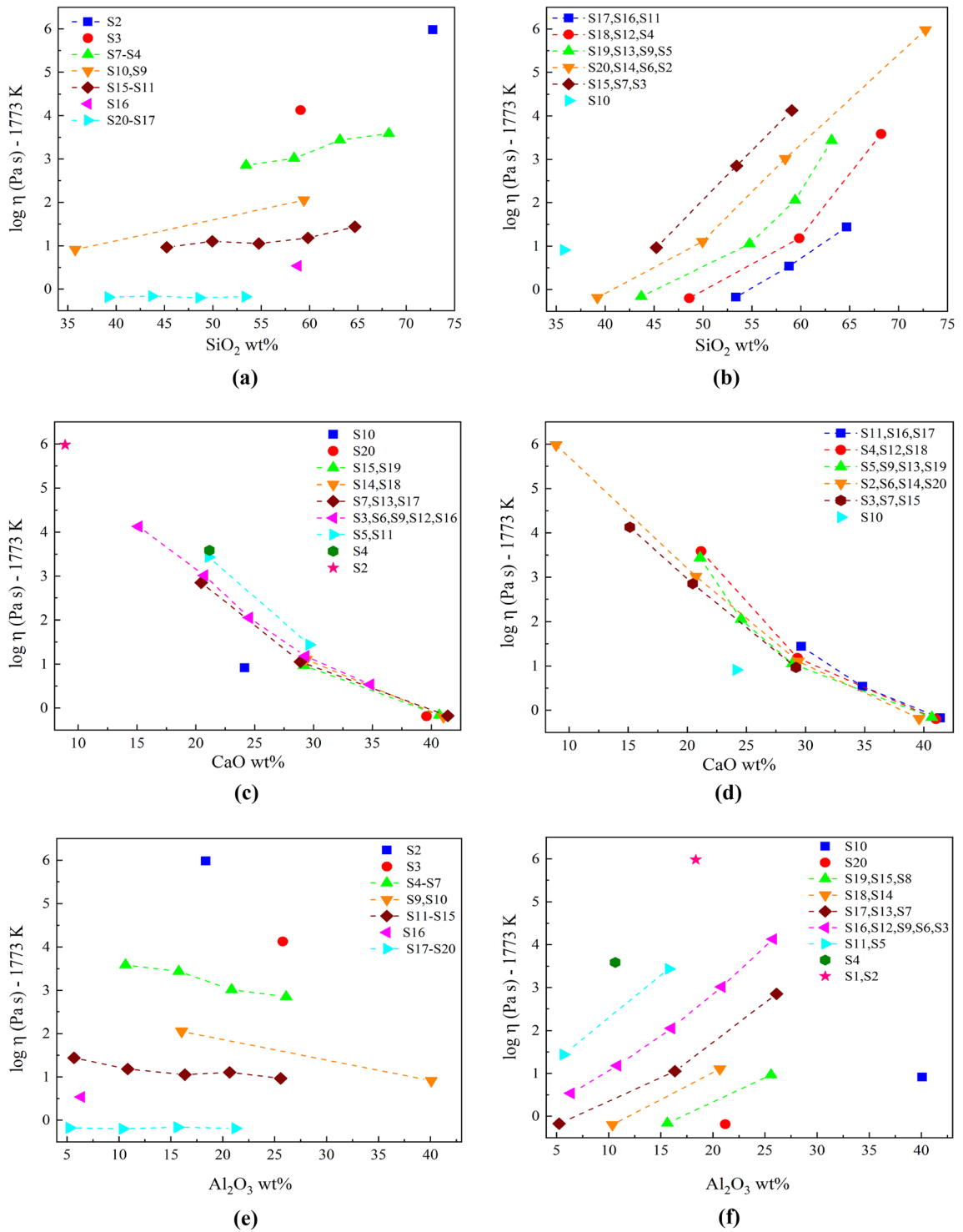


Fig. 7— $\log \eta$ (Pa s)^[53] vs SiO₂ wt pct (a) low to high contents of CaO wt pct and (b) low to high contents of Al₂O₃ wt pct. $\log \eta$ (Pa s)^[53] vs CaO wt pct (c) low to high contents of SiO₂ wt pct and (d) low to high contents of Al₂O₃ wt pct. $\log \eta$ (Pa s)^[53] vs Al₂O₃ wt pct for (e) low to high contents of CaO wt pct and (f) low to high contents of SiO₂ wt pct.

solid lines while the experimental viscosity values are shown by markers. Figure 11 demonstrates that the prediction of the Raman-structure model given by Eq. [4] is in good agreement to the experimental slag viscosity over a wide range of slag compositions and temperatures.

In Figures 12(a) through (c), experimental viscosity values are compared with the models proposed by Iida,^[58] Mills,^[2] and Giordano,^[59] respectively. The models depend on temperature and the structural chemical parameters, namely basicity, optical basicity, and NBO/T. The Iida model overestimates the viscosity

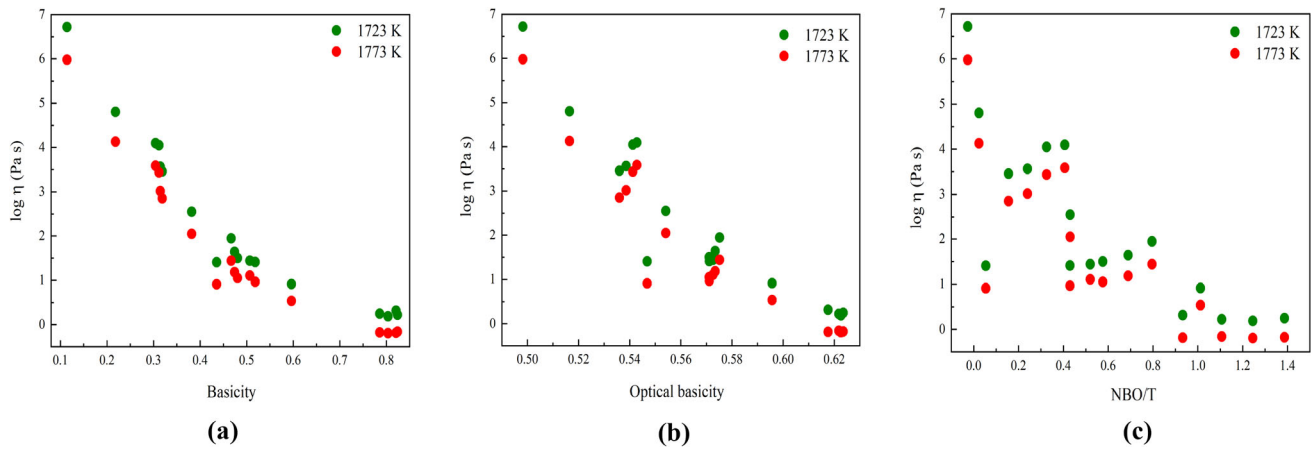


Fig. 8— $\log \eta$ (Pa s)^[53] vs (a) Basicity, (b) Optical basicity, and (c) NBO/T.

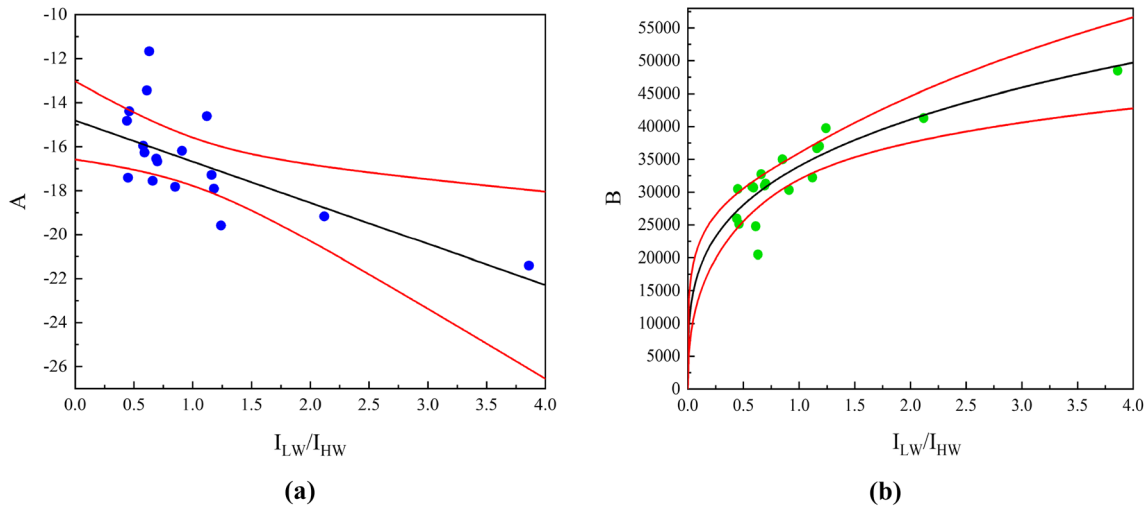


Fig. 9—(a) and (b) A and B parameters in the Arrhenius equation vs R (I_{LW}/I_{HW}), respectively. Red lines show 95 pct confidence band (Color figure online).

Table IV. Parameters of Arrhenius Relation Applied on Log η (Pa s) vs Temperature (K)

Slag	Arrhenius Parameters		Slag	Arrhenius Parameters	
	A	B		A	B
S1			S11	-15.9	30833
S2	-21.4	48482	S12	-16.3	30700
S3	-19.2	41312	S13	-17.5	32725
S4	-14.6	32240	S14	-16.6	31279
S5	-17.3	36713	S15	-16.5	30988
S6	-17.9	36987	S16	-13.4	24773
S7	-19.6	39742	S17	-11.7	20471
S8			S18	-14.4	25142
S9	-17.8	35004	S19	-14.8	25959
S10	-16.2	30320	S20	-17.4	30470

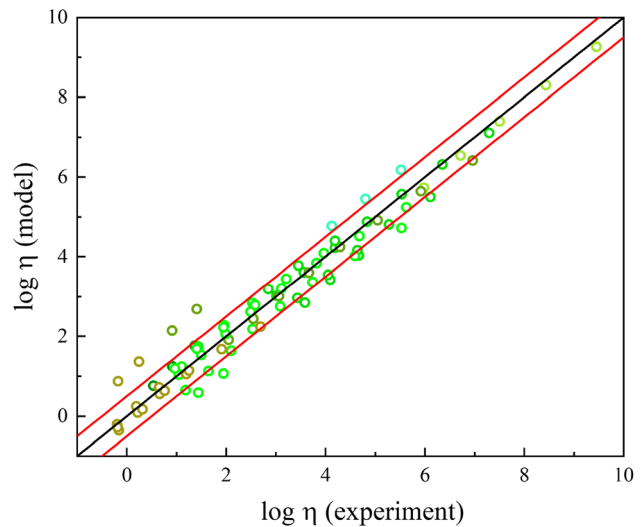


Fig. 10—Experimental values of viscosity against predicted values. Red lines show an envelop of ± 0.5 log units.

values especially for slags containing high content of SiO_2 , e.g., slag S2, while the Mills model underestimates the viscosity data for most of the slag compositions. The

Giordano model predicts the viscosity values closer to the experimental measurements for all compositions and temperatures except for slags S2, S3, and S10 with the lowest NBO/T values. For the current dataset, the proposed model based on the R parameter appears to provide a better prediction of viscosity.

IV. CONCLUSION

In this paper, the relationship between slag structure and viscosity is studied for a group of 20 synthetic slags in the $\text{SiO}_2\text{-CaO-Al}_2\text{O}_3$ system using the Raman spectra measurements. The effect of SiO_2 , CaO , Al_2O_3 oxides on slag structural parameters derived from Raman spectra, namely R and C_{HW} , and slag viscosity is discussed in detail. The role of Al_2O_3 as an amphoteric oxide is

demonstrated using Raman parameters while the corresponding behavior cannot be found in the analysis of viscosity data presented here.

An empirical viscosity model is developed for this group of slags where the temperature dependency of viscosity is expressed through the Arrhenius relation. The model depends on a single structure-related Raman parameter (R). Here, R is obtained as the ratio of intensity heights (I) for the two main bands of low wavenumber (LW) and high wavenumber (HW) in Raman spectra ($R = I_{\text{LW}}/I_{\text{HW}}$) in the range of 200 to 1300 cm^{-1} . The model relies on four adjustable parameters to convert measured R values to temperature dependent viscosity values. Comparing the model predictions and experimental observations, a good agreement between the model and measured values of viscosity is found. Our findings offer this Raman-based model to be a promising tool for the prediction of viscosity of slags using only one parameter in high-temperature metallurgical processes.

ACKNOWLEDGMENTS

This work is funded by SFI Metal Production, Centre for Research-based Innovation, 237738. Financial support from the Research Council of Norway and the partners of SFI Metal Production are gratefully acknowledged.

FUNDING

Open access funding provided by NTNU Norwegian University of Science and Technology (incl St. Olavs Hospital - Trondheim University Hospital).

CONFLICT OF INTEREST

On behalf of all authors, the corresponding author states that there is no conflict of interest.

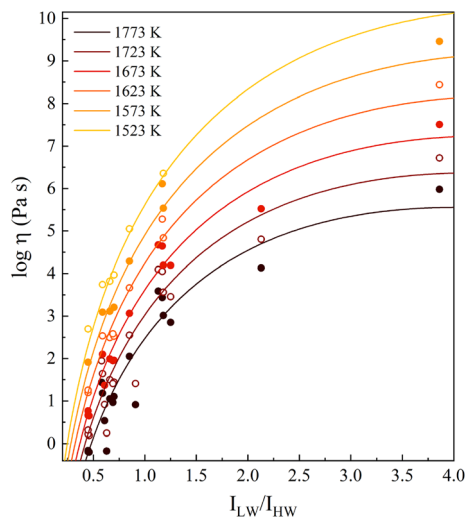


Fig. 11—Predicted isothermal viscosity (1523 to 1773 K) obtained using Eq. [4] for the range of 0 to 4 of R ($I_{\text{LW}}/I_{\text{HW}}$) (solid lines). Experimental viscosity measurements, $\log \eta$ (Pa s)^[53] (markers).

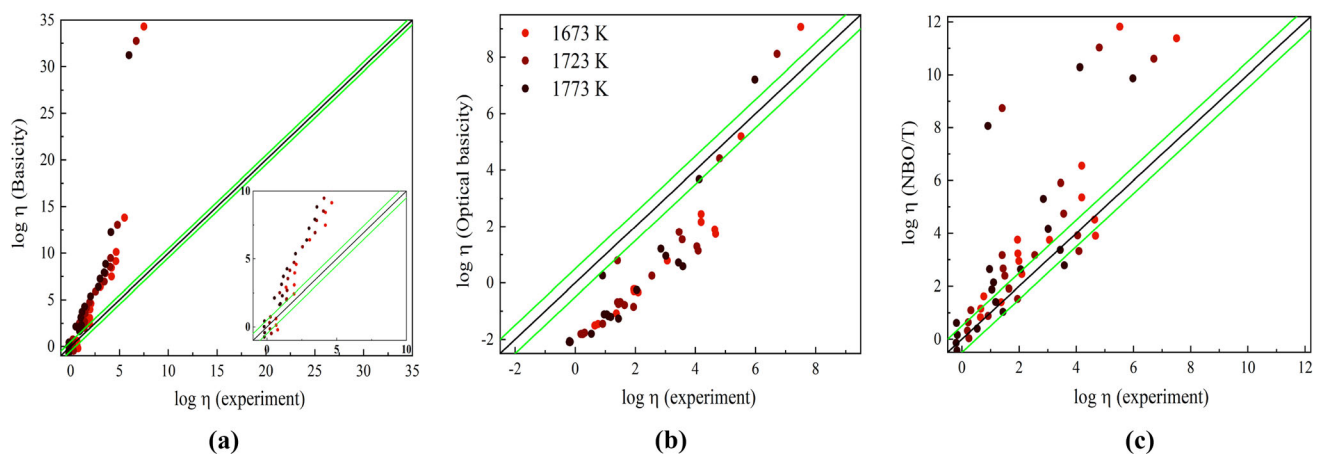


Fig. 12—Comparison of experimental values of viscosity against predicted values through (a) Basicity,^[58] (b) Optical basicity,^[2] and (c) NBO/ T ^[59]

OPEN ACCESS

This article is licensed under a Creative Commons Attribution 4.0 International License, which permits use, sharing, adaptation, distribution and reproduction in any medium or format, as long as you give appropriate credit to the original author(s) and the source, provide a link to the Creative Commons licence, and indicate if changes were made. The images or other third party material in this article are included in the article's Creative Commons licence, unless indicated otherwise in a credit line to the material. If material is not included in the article's Creative Commons licence and your intended use is not permitted by statutory regulation or exceeds the permitted use, you will need to obtain permission directly from the copyright holder. To view a copy of this licence, visit <http://creativecommons.org/licenses/by/4.0/>.

REFERENCES

1. S.E. Olsen, M. Tangstad, T. Lindstad, *Production of Manganese Ferroalloys* (Tapir Akademisk Forlag, Trondheim, 2007).
2. K. Mills, S. Sridhar, *Ironmak. Steelmak.* **26**, 262–268 (1999).
3. W.H. Kim, I. Sohn, D.J. Min, *Steel Res. Int.* **81**, 735–741 (2010).
4. J. Nell, C. Joubert, *INFACON* **13**, 265–272 (2013).
5. M. Tangstad, M. Ksiazek, J.E. Andersen, *Silicon Chem. Solar Ind.* **12**, 19–28 (2014).
6. M.B. Folstad, M. Ksiazek, M. Tangstad, *Silicon Chem. Solar Ind.* **15**, 119–127 (2020).
7. I. Sohn, D.J. Min, *Steel Res. Int.* **83**, 611–630 (2012).
8. Z.-G. Yu, H.-Y. Leng, L.-J. Wang, K.-C. Chou, *Ceram. Int.* **45**, 7180–7187 (2019).
9. Y. Hou, G.-H. Zhang, K.-C. Chou, D. Fan, *Metall. Mater. Trans. B* **51**, 985–1002 (2020).
10. R. Zhang, Y. Min, Y. Wang, X. Zhao, J.X. Jia, C.J. Liu, *Energy Fuels* **34**, 8129–8138 (2020).
11. Z. Wang, S. Huang, G. Wen, Q. Liu, P. Tang, *J. Mol. Liq.* **324**, 114697 (2021).
12. B.O. Mysen, D. Virgo, C.M. Scarfe, *Am. Mineral* **65**, 690–710 (1980).
13. B.O. Mysen, *Am. Mineral* **70**, 88–105 (1985).
14. K. Mills, *Slag Atlas*, 2nd edn. (Verlag Stahleisen GmbH, Düsseldorf, 1995).
15. Y. Waseda, J. Toguri, *The Structure and Properties of Oxide Melts* (World Scientific Publishing, Singapore, 1998).
16. B.O. Mysen, D. Virgo, F.A. Seifert, *Rev. Geophys.* **20**, 353 (1982).
17. K.C. Mills, *ISIJ Int.* **33**, 148–155 (1993).
18. J.H. Park, D.J. Min, H.S. Song, *Metall. Mater. Trans. B* **35**, 269–275 (2004).
19. K.C. Mills, *J. South. Afr. Inst. Min. Metall.* **111**, 649–658 (2011).
20. J.H. Park, *Metall. Mater. Trans. B* **44**, 938–947 (2013).
21. J. Kline, Structures of CaO-SiO₂, CaO-MgO-SiO₂ and CaO-Al₂O₃-SiO₂ slags and with the addition of B₂O₃: A Raman spectroscopic study. PhD Thesis, Norwegian University of Science and Technology (2013).
22. T.S. Kim, J.H. Park, *ISIJ Int.* **54**, 2031–2038 (2014).
23. J. Kline, M. Tangstad, G. Tranell, *Metall. Mater. Trans. B* **46**, 62–73 (2015).
24. Z. Chen, H. Wang, Y. Sun, L. Liu, X. Wang, *Metall. Mater. Trans. B* **50**, 2930–2941 (2019).
25. S. Haghdani, M. Tangstad, K.E. Einarsrud, *INFACON* **16**, 1–8 (2021).
26. B.O. Mysen, P. Richet, *Silicate Glasses and Melts: Properties and Structure* (Elsevier, Amsterdam, 2005).
27. S. Rossano, B. Mysen, Raman Spectroscopy of silicate glasses and melts in geological systems, in *Raman Spectroscopy Applied to Earth Sciences and Cultural Heritage*. ed. by J. Dubessy, M.C. Caumon, F. Rull (Mineralogical Society of Great Britain and Ireland, London, 2012), pp. 319–364.
28. D.R. Neuville, D. de Ligny, G.S. Henderson, *Rev. Mineral. Geochim.* **78**, 509–541 (2014).
29. A.K. Yadav, P. Singh, *RSC Adv.* **5**, 67583–67609 (2015).
30. W.J. Malfait, Chapter 8-Vibrational properties of glasses and melts, in *Magmas Under Pressure*. ed. by Y. Kono, C. Sanloup (Elsevier, Amsterdam, 2018), pp. 211–236.
31. D. Giordano, J.K. Russell, D. González-García, D. Bersani, D.B. Dingwell, C. Del Negro, *Remote Sens.* **12**, 805 (2020).
32. H.D. Weymann, *Koll. Zeitschr. Zeitschr. Polym.* **181**, 131–137 (1962).
33. H. Vogel, *Phys. Z.* **22**, 645–646 (1921).
34. G.S. Fulcher, *J. Am. Ceram. Soc.* **8**, 339–355 (1925).
35. G. Tammann, W. Hesse, *Z. Anorg. Allg. Chem.* **156**, 245–257 (1926).
36. G.J. Browning, G.W. Bryant, H.J. Hurst, J.A. Lucas, T.F. Wall, *Energy Fuels* **17**, 731–737 (2003).
37. J.K. Russell, D. Giordano, *Geochim. Cosmochim. Acta* **69**, 5333–5349 (2005).
38. P.V. Riboud, Y. Roux, L.-D. Lucas, H. Gaye, *Fachber. Huttenpraxis Metallweiterver* **19**, 859–869 (1981).
39. G. Urbain, *Steel Res. Int.* **58**, 111–116 (1987).
40. A. Kondratiev, E. Jak, *Metall. Mater. Trans. B* **32**, 1015–1025 (2001).
41. D. Giordano, J.K. Russell, D.B. Dingwell, *Earth Planet. Sci. Lett.* **271**, 123–134 (2008).
42. M.A. Duchesne, A.M. Bronsch, R.W. Hughes, P.J. Masset, *Fuel* **114**, 38–43 (2013).
43. L. Zhang, S. Jahanshahi, *Metall. Mater. Trans. B* **29**, 177–186 (1998).
44. L. Zhang, S. Jahanshahi, *Scand. J. Metall.* **30**, 364–369 (2001).
45. A. Kondratiev, E. Jak, *Metall. Mater. Trans. B* **36**, 623–638 (2005).
46. E. Yazhenskikh, K. Hack, M. Müller, *Calphad* **30**, 270–276 (2006).
47. D. Giordano, J.K. Russell, *Earth Planet. Sci. Lett.* **501**, 202–212 (2018).
48. M. Mercier, A.D. Muro, D. Giordano, N. Me'trich, P. Lesne, M. Pichavant, B. Scaillet, R. Cloccchiatti, G. Montagnac, *Geochim. Cosmochim. Acta* **73**, 197–217 (2009).
49. M. Mercier, A.D. Muro, N. Me'trich, D. Giordano, O. Belhadj, C.W. Mandeville, *Geochim. Cosmochim. Acta* **74**, 5641–5656 (2010).
50. D. Giordano, D. González-García, J.K. Russell, S. Raneri, D. Bersani, L. Fornasini, D.D. Genova, S. Ferrando, M. Kaliwoda, P.P. Lottici, M. Smit, D.B. Dingwell, *J. Raman Spectrosc.* **51**, 1822–1838 (2020).
51. D.J. Min, F. Tsukihashi, *Met. Mater. Int.* **23**, 1–19 (2017).
52. M. Sajid, C. Bai, M. Aamir, Z. You, Z. Yan, X. Lv, *ISIJ Int.* **59**, 1153–1166 (2019).
53. J.S. Machin, T.B. Yee, *J. Am. Ceram. Soc.* **31**, 200–204 (1948).
54. M. Wojdyr, *J. Appl. Cryst.* **43**, 1126–1128 (2010).
55. D.R. Neuville, B.O. Mysen, *Geochim. Cosmochim. Acta* **60**, 1727–1737 (1996).
56. P. McMillan, *Am. Mineral.* **69**, 622–644 (1984).
57. B. Mysen, P. Richet, *Structure of Metal Oxide-Silica Systems* (Elsevier, Amsterdam, 2019), pp. 223–262.
58. T. Iida, H. Sakai, Y. Kita, K. Shigeno, *ISIJ Int.* **40**, 110–114 (2000).
59. D. Giordano, D.B. Dingwell, *Earth Planet. Sci. Lett.* **208**, 337–349 (2003).

Publisher's Note Springer Nature remains neutral with regard to jurisdictional claims in published maps and institutional affiliations.